Materials Research Bulletin 47 (2012) 1204–1211

Contents lists available at SciVerse ScienceDirect

Materials Research Bulletin

journal homepage: www.elsevier.com/locate/matresbu

Electrical conductivity of $Ca_{1-x}Sr_xTi_{0.65}Fe_{0.35}O_{3-\delta}$, $x = 0$, 0.5 and 1, polycrystalline compounds in the 300–500 K range

R. Muccillo *, J.R. Carmo

Center of Science and Technology of Materials, Energy and Nuclear Research Institute, Travessa R 400, Cidade Universitaria, S. Paulo, SP 05508-900, Brazil

ARTICLE INFO

Article history:
Received 30 July 2011
Received in revised form 12 January 2012
Accepted 27 January 2012
Available online 7 February 2012

Keyword:
A. Ceramics
B. Chemical synthesis
C. Atomic force microscopy
D: Electrical properties

ABSTRACT

Bulk and grain boundary electrical conductivity of oxygen deficient $Ca_xSr_{1-x}Ti_{0.65}Fe_{0.35}O_{3-\delta}$, $x = 0$, 0.5 and 1.0, polycrystalline specimens were evaluated by impedance spectroscopy measurements in the 5 Hz–13 MHz frequency range from 300 to 500 K. The ceramic powders were synthesized by solid state reaction and by a chemical route, the polymeric precursor technique. The X-ray diffraction of the samples at room temperature shows the following perovskite crystalline structures: cubic for $x = 0$ and orthorhombic for $x = 0.5$ and 1.0. The impedance plots are composed of two semicircles ascribed to grains (bulk) and interfaces (grain boundaries) contributions. The impedance data show that sintered pellets using powders prepared by solid state synthesis present higher intergranular and intragranular resistivity values than pellets prepared by the chemical route. Observations of scanning probe microscopy topographic images of the surfaces of the sintered pellets show evident differences between the grain morphology of the pellets prepared with powders synthesized by the two routes.

1. Introduction

Many studies are focused in the $SrTiO_3$ (STO) compound mainly for its thermoelectric behavior. STO-based oxides are a promising group of *n*-type thermoelectric materials because they exhibit excellent electronic transport properties and are basically stable at high temperatures [1]. Successful aliovalent doping yields compounds with different interesting properties either in bulk ceramic or thin/thick film specimens.

More recently, several studies on $SrTi_{1-x}Fe_xO_{3-\delta}$ (STFO) compounds were undertaken looking for suitable compositions for use in temperature independent oxygen automotive lambda sensors [2–9]. The main reported conclusions are that these compounds exhibit mixed ionic–electronic conductivity at elevated temperatures (>550 °C), predominant *n*-type electronic conductivity at low oxygen pressures, ionic conductivity at intermediate oxygen pressures, and *p*-type electronic conductivity at high oxygen pressures, and that the oxygen vacancy concentration is independent on the partial pressure of oxygen [5]. The electrical resistance of these compounds was studied in the 700–1000 °C in the oxygen partial pressure range from 10^{-4} to 1 bar [4]. Fe ions are considered to be one of the main constituents of the $SrTi_{0.65}Fe_{0.35}O_{3-\delta}$ compound and not just an acceptor impurity dopant with such a high level [5]. Moreover, the composition $SrTi_{0.65}Fe_{0.35}O_{3-\delta}$, in which 0.35 mol of Ti is replaced by Fe, shows a zero temperature coefficient of resistance (zero-TCR), i.e., the electrical response depends only on the partial pressure of oxygen in a certain temperature range, being consequently the optimized composition for a temperature independent oxygen sensor [2,3]. For this reason, electrical measurements on compositions with 0.35 mol Fe are here reported.

An interesting approach to the study of the electrical behavior of polycrystalline compounds is the electrochemical impedance spectroscopy technique. There are several complex formalisms to analyze the impedance spectroscopy data. Here we expose the data using two plots: the impedance plot, $[Z''(\omega) \times Z'(\omega)]$, and the Bode reactance plot, $[Z''(\omega) \times \log f]$. The former highlights the resistive components and the latter allows for visualizing better the frequency dependence [10]. The impedance plot is composed of one or more overlapped semicircles, which may be assigned to different contributions to the electrical resistivity due to bulk (grains) and to interfaces (mainly grain boundaries) when the compound is a polycrystalline ceramic [11]. Bode plots are either $|Z(\omega)|$ or $Z''(\omega)$ as a function of the logarithm of the frequency. Depending on the temperature and on the frequency range the experiment is performed, the impedance plot $[-Z''(\omega) \times Z'(\omega)]$ usually presents in the complex plane two visually separated semicircles [10,12], each one being represented by an equivalent circuit composed of a resistor in parallel with a capacitance ($R//C$). The high-frequency semicircle is due to the electrical response of the bulk of the polycrystalline specimen, whereas the low frequency one is assigned to the electrical properties of the grain

* Corresponding author. Tel.: +55 11 31339203; fax: +55 11 31339276.
E-mail address: muccillo@usp.br (R. Muccillo).

0025-5408/$ – see front matter © 2012 Elsevier Ltd. All rights reserved.
doi:10.1016/j.materresbull.2012.01.029

boundaries, which may act as blockers to charge carriers. The capacitance may be represented by a constant phase element, CPE, when the center of the semicircle lies below the Z' axis. The impedance of a CPE is given by $Z_{CPE} = Q^{-1}(j\omega)^{-\alpha}$, $0 \leq \alpha \leq 1$, $\alpha = 1$ representing a pure capacitance, given by $Z_C = 1/(j\omega C)$ [13]. For the estimation of capacitances associated with impedance arcs, the equation $Cps = (RQ)^{1/\alpha}/R$ is used [14,15]. R is the resistance determined at the intersection of the impedance arc with the real axis. The impedance spectroscopy technique allows, at least to a first approximation, the separation of impedance contributions from grain interior (bulk) and grain boundaries [16].

Detailed impedance analysis of bulk conductivity of Ni-doped $SrTiO_3$ and of grain boundaries in acceptor (Ni, Fe and Al) doped $SrTiO_3$ has been given by Waser [17,18]. Oxygen vacancies were suggested as the mobile species for the electric conduction [17], and the high resistive grain boundary layer was ascribed to a space charge depletion layer [18]. The behavior of the electrical conduction at grain boundaries in polycrystalline $SrTiO_3$ is usually considered to be due to space-charge layers in the bulk regions adjacent to the interfaces [19]. Charge and mass may be blocked at these interfaces. For single crystalline $SrTiO_3$ specimens, oxygen vacancies at the grain boundaries are considered responsible for the intrinsic correlation between microstructure and impedance [20]. Impedance spectroscopy experiments were already performed in $SrTiO_3$ polycrystalline specimens with different amounts of Fe_2O_3, 1%, 2% and 3% [21] and with 0.05, 0.07, 0.10, 0.15, 0.2, 0.4 and 0.5 mol [22]. The electrical behavior of grain boundaries as well as the grain growth was found to strongly depend on the Fe content. A detailed experimental work was also reported concerning the electronic structure, the defect chemistry and the transport properties of $SrTiFe_xO_{3-y}$ solid solutions, oxide ion conductivity being proposed to be predominant at intermediate oxygen partial pressures [5].

Recent applications of strontium titanate based materials have been reported on anode for Solid Oxide Fuel Cells due to their electrical behavior and mechanical compatibility with the yttria-stabilized zirconia solid electrolyte [23,24].

Many research works have also been carried out in $CaTiO_3$ (CTO), which has a distorted perovskite structure with orthorhombic symmetry at room temperature. CTO shows the ability of forming solid solutions with a large number of oxides and, therefore, many compounds have been synthesized for different applications [25–31]. Bulk and grain boundary conductivity of $Ca_{0.97}Ti_{1-x}Fe_xO_{3-\delta}$ ($x = 0$, 0.01, 0.035, 0.07 and 0.15) materials show that the electrical conductivity increases with Fe addition with a behavior similar to Fe-doped strontium titanate [32].

Here a careful examination was pursued on the analysis of impedance data of $SrTi_{0.65}Fe_{0.35}O_{3-\delta}$, $CaTi_{0.65}Fe_{0.35}O_{3-\delta}$ and $Ca_{0.5}Sr_{0.5}Ti_{0.65}Fe_{0.35}O_{3-\delta}$ synthesized by two techniques, namely, the polymeric precursor (chemical route) and the solid state reaction (ceramic route) techniques. The ionic radii of Ca^{2+} and Sr^{2+} are 1.48 and 1.58 Å, respectively, suggesting a favorable accommodation of the Ca^{2+} ion for Sr^{2+}in the ABO_3 structure of the perovskite lattice. The large content of Fe substitution for Ti in $SrTiO_3$ and in $CaTiO_3$ creates oxygen vacancies, enhancing their ionic conductivity relatively to the undoped titanates. Impedance, Bode and Arrhenius plots are presented.

2. Experimental

$Ca_{1-x}Sr_xTi_{0.65}Fe_{0.35}O_{3-\delta}$, $x = 0$, 0.5 and 1 (hereafter CTFO, CSTFO and STFO), powders were prepared according to two techniques: (1) solid state reaction, consisting in mixing stoichiometric amounts of $CaCO_3$, $SrCO_3$, TiO_2 and Fe_2O_3 (all from Alfa Aesar) for 2 h in alcoholic medium in a turbula mixer, drying the mixture, and promoting solid solution formation by calcination in air at 1250 °C for 15 h [33]. Simultaneous thermogravimetry and differential thermal analyses, not reported here, were carried out in a Netzsch STA409E equipment in the room temperature – 1550 °C-room temperature cycle under flowing synthetic air, to be sure that the heat treatment at 1250 °C completely reduces both carbonates; (2) polymeric precursor technique, consisting of mixing under stirring at 100 °C stoichiometric amounts of calcium carbonate ($CaCO_3$), strontium carbonate ($SrCO_3$), iron nitrate ($Fe(NO_3)_3{\cdot}9H_2O$) and titanium isopropoxide ($C_{12}H_{28}O_4Ti$) (all from Alfa Aesar), in an acid solution ($H_2O/HNO_3 = 20/1$); after stirring for 20 min, citric acid and ethylene glycol were added stepwise to the solution under stirring for 30 min, yielding a highly viscous resin, which had the organics burnt out after calcination at 200, 250 and 300 °C for 2 h and at 800 °C for 5 h. These temperature profiles were chosen after evaluating the thermogravimetric analysis of the resins.

X-ray diffraction experiments were carried out in all compositions in a Bruker-AXS D8 Advance X-ray diffractometer with θ–2θ Bragg–Brentano configuration with Cukα radiation with Ni filter, 40 kV–40 mA, in the 10–90° 2θ range, 0.05° step size, and 5 s counting time per step.

The powders of each composition, namely, STFO, CTFO and CSTFO, prepared by both the solid state synthesis (hereafter SS) and the polymeric precursor (PP) technique, were pressed to 12 mm diameter disks (uniaxially at 96 MPa, followed by isostatically at 210 MPa). Sintering was performed in air in a programmable Lindberg-BlueM furnace at 1300 °C for 2 h, 5 °C/min heating and cooling rates.

For the impedance measurements, thin silver layers were deposited in the parallel surfaces of the sintered pellets. These electrodes are known to give rise to negligible electrode polarization contribution in the impedance plot and, consequently, do not produce overlapping with the grain boundary arc in the low frequency region. The impedance response of the polycrystalline specimens was determined with a 4192A Hewlett Packard LF Impedance Analyzer connected to a series 360 Hewlett Packard Controller over the frequency range of 5 Hz–13 MHz, with signal amplitude of 100 mV. Some measurements were performed with 50, 100, 200 and 500 mV to determine the linear response region and the lowest input signal that gives rise to the less noisy electrical responses. Measurements were made in the temperature range $300 < T(K) < 500$ at atmospheric air pressure. For each impedance measurement, the temperature was expected to be constant within 0.5 °C. The $[-Z''(\omega) \times Z'(\omega)]$ impedance plots were deconvoluted using a special software to obtain the intergranular (grain boundary – gb) and intragranular (bulk or grain – g) electrical resistances, frequencies and decentralization angles [34].

The polished surfaces of the sintered pellets were observed in a scanning probe microscope (Jeol JSPM-5200, contact mode, dynamic force topography images, 10 μm × 10 μm scanning area). Polishing was done sequentially with silicon carbide powders and 30, 15, 6, 3 and 1 μm diamond pastes, with further ultrasonic cleaning with isopropanol. The polished specimens were thermally etched at 1200 °C/20 min to reveal the surface grain boundaries.

3. Results and discussion

Fig. 1 shows the results of the X-ray diffraction experiments on STFO, CTFO and CSTFO powders prepared by the solid state synthesis and by the polymeric precursor technique.

Rietveld analyses performed with the GSAS software [35] of X-ray diffraction data of the compounds synthesized by the polymeric precursor technique give the following values for the lattice parameters: perovskite orthorhombic with $a = 5.41309$ (0.00004) Å, $b = 7.65496$ (0.00006) Å and $c = 5.41091$ (0.00008) Å

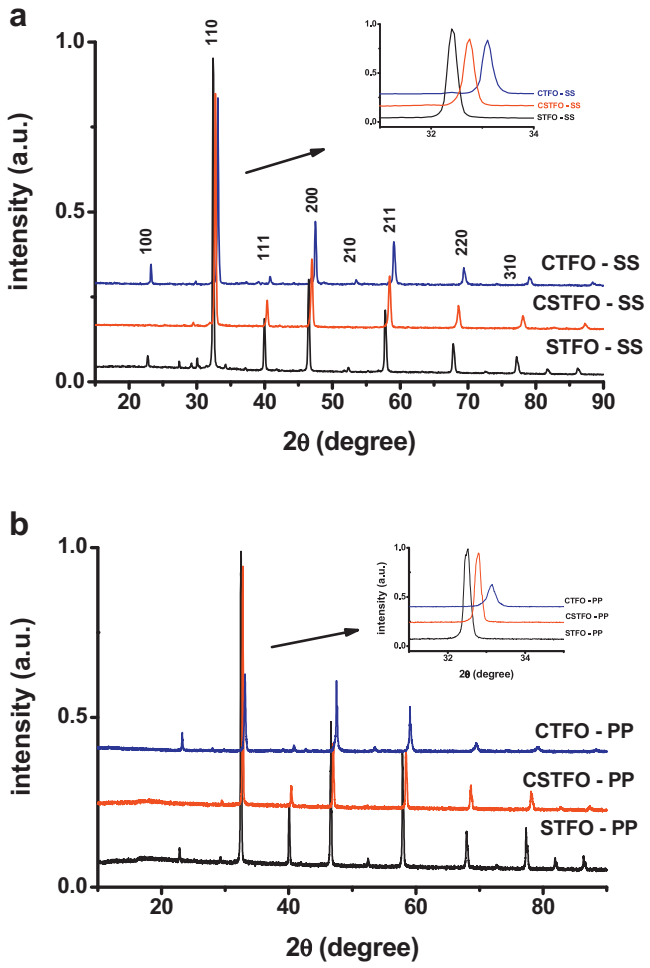

Fig. 1. X-ray diffraction patterns of $SrTi_{0.65}Fe_{0.35}O_{3-\delta}$ (STFO), $CaTi_{0.65}Fe_{0.35}O_{3-\delta}$ (CTFO) and $Ca_{0.5}Sr_{0.5}Ti_{0.65}Fe_{0.35}O_{3-\delta}$ (CSTFO) powders obtained by solid state synthesis (SS) (a) and the polymeric precursor technique (PP) (b).

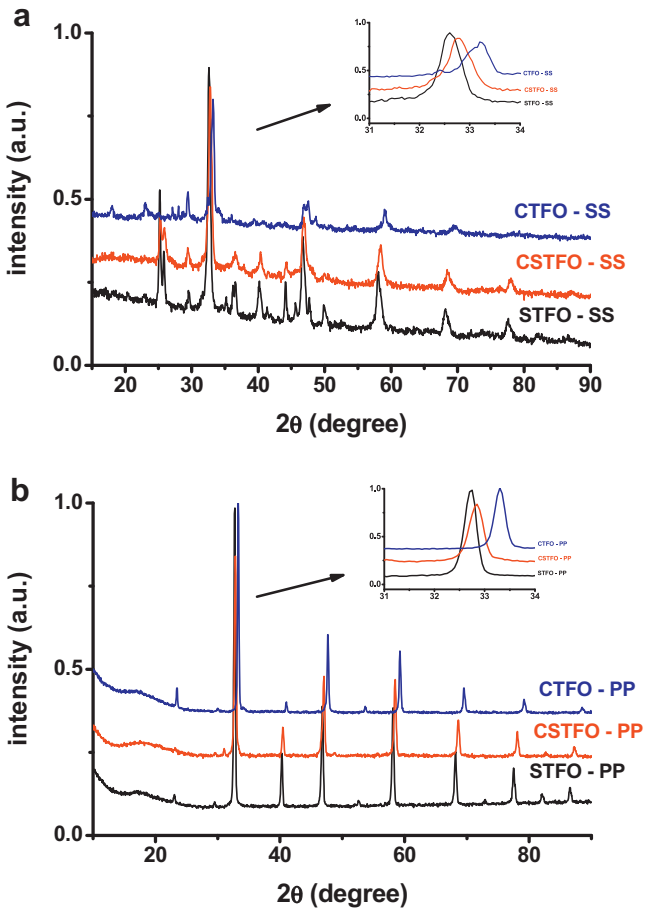

Fig. 2. X-ray diffraction patterns of $SrTi_{0.65}Fe_{0.35}O_{3-\delta}$ (STFO), $CaTi_{0.65}Fe_{0.35}O_{3-\delta}$ (CTFO) and $Ca_{0.5}Sr_{0.5}Ti_{0.65}Fe_{0.35}O_{3-\delta}$ (CSTFO) sintered pellets prepared with powders obtained by the solid state synthesis (SS) (a) and the polymeric precursor (PP) technique (b).

for $CaTi_{0.65}Fe_{0.35}O_{3-\delta}$; perovskite orthorhombic with $a = 5.47077$ (0.00004) Å, $b = 5.47163$ (0.00005) Å and $c = 7.73996$ (0.00006) Å for $Ca_{0.5}Sr_{0.5}Ti_{0.65}Fe_{0.35}O_{3-\delta}$; perovskite cubic with $a = b = c = 3.90141$ (0.00001) Å for $SrTi_{0.65}Fe_{0.35}O_{3-\delta}$. The compounds prepared by solid state synthesis, on the other hand, have perovskite cubic structure ($SrTi_{0.65}Fe_{0.35}O_{3-\delta}$ and $CaTi_{0.65}Fe_{0.35}O_{3-\delta}$) and a mixture of perovskite orthorhombic phases ($Ca_{0.5}Sr_{0.5}Ti_{0.65}Fe_{0.35}O_{3-\delta}$). The X-ray diffraction patterns of powders obtained by solid state synthesis show several extra reflections due to the non-completeness of the synthesis reaction. The sharp and single diffraction peaks in the X-ray diffraction patterns of the powders synthesized by the polymeric precursor route, on the other hand, show that these powders present single cubic perovskite phase, as expected from a chemical synthesis. The insets in these figures show that there is a shift of the peak positions towards higher angles (Sr, SrCa, Ca), indicating a decrease in lattice parameter, when replacing the larger ionic radius Sr^{2+} (158 pm) for the smaller ionic radius Ca^{2+} (148 pm) in the crystal lattice.

Fig. 2 shows the results of the X-ray diffraction measurements on the surfaces of STFO, CTFO and CSTFO sintered pellets prepared with powders obtained by the solid state synthesis and by the polymeric precursor technique.

The $SrTi_{0.65}Fe_{0.35}O_{3-\delta}$ and the $Ca_{0.5}Sr_{0.5}Ti_{0.65}Fe_{0.35}O_{3-\delta}$ pellets have the same structure, cubic perovskite, while the $CaTi_{0.65}Fe_{0.35}O_{3-\delta}$ pellet has the orthorhombic structure. The partial substitution of Ca for Sr does not modify the original cubic perovskite structure of the strontium titanate, besides modifying the lattice parameter according to Vegard's law. Similarly to the case of the powders, the diffraction patterns of the sintered pellets prepared with SS powders still present extra reflections due to second phases resulting from the incomplete formation of the expected phase. The opposite is true for the sintered PP pellets, which are all single phase.

Figs. 3–5 show impedance plots of $SrTi_{0.65}Fe_{0.35}O_{3-\delta}$ – STFO, $CaTi_{0.65}Fe_{0.35}O_{3-\delta}$ – CTFO and $Ca_{0.5}Sr_{0.5}Ti_{0.65}Fe_{0.35}O_{3-\delta}$ – CSTFO sintered pellets, respectively. Electrical resistivity values, $\rho = R{\cdot}S/t$ are plotted, taking into account the geometric factors (electrode area S/thickness t). The imaginary component $Z''(\omega)$ is plotted as a function of the real component $Z'(\omega)$ of the complex impedance $Z^*(\omega) = Z'(\omega) - jZ''(\omega)$. A sintered ceramic usually contains grains and interfacial boundary layers (largely grain boundaries). Both grains and grain boundaries give rise to the electrical contribution to the impedance. The sintered compounds here presented are typical examples. Above room temperature the impedance plots are deconvoluted into two semicircles, one due to the response of grain boundaries (intergranular, low frequency region) and the other to the response of grains (intragranular – high frequency). The Bode representation of the imaginary component of the impedance is shown in the same figure, along with the $[Z''(\omega) \times Z'(\omega)]$ plots, only for two temperatures of measurement (~65 and ~100 °C), for the sake of clarity. The values in the ordinate were normalized to 1.0. The Bode representation allows for a better view in the frequency domain of the two components of the impedance spectroscopy data.

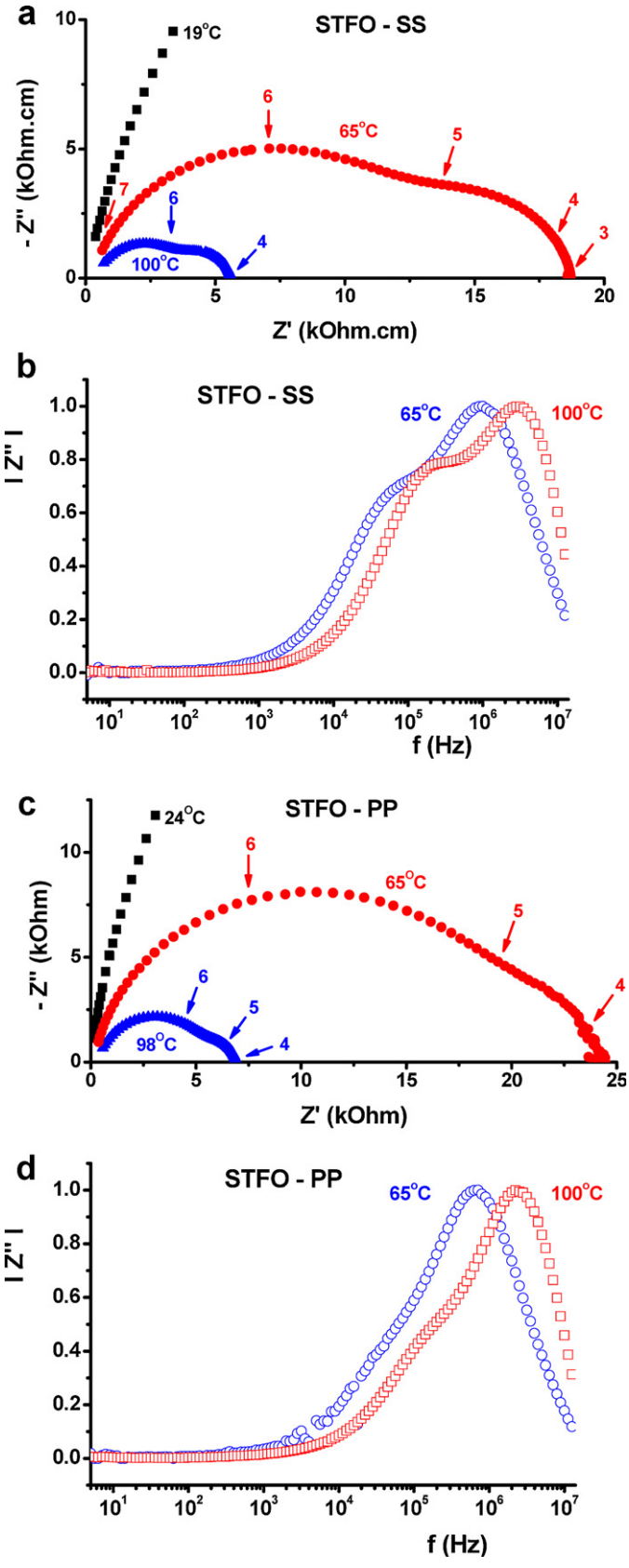

Fig. 3. (a) and (c) Impedance spectroscopy plots in the 5 Hz–13 MHz frequency range of polycrystalline $SrTi_{0.65}Fe_{0.35}O_{3-\delta}$ (STFO) at several temperatures. The numbers are the logarithm of frequency. Inset: zoom of the high frequency region. (b) and (d) Bode plots at 65 and 100 °C. (a) and (b) Solid state synthesis (SS); (c) and (d) polymeric precursor (PP) technique.

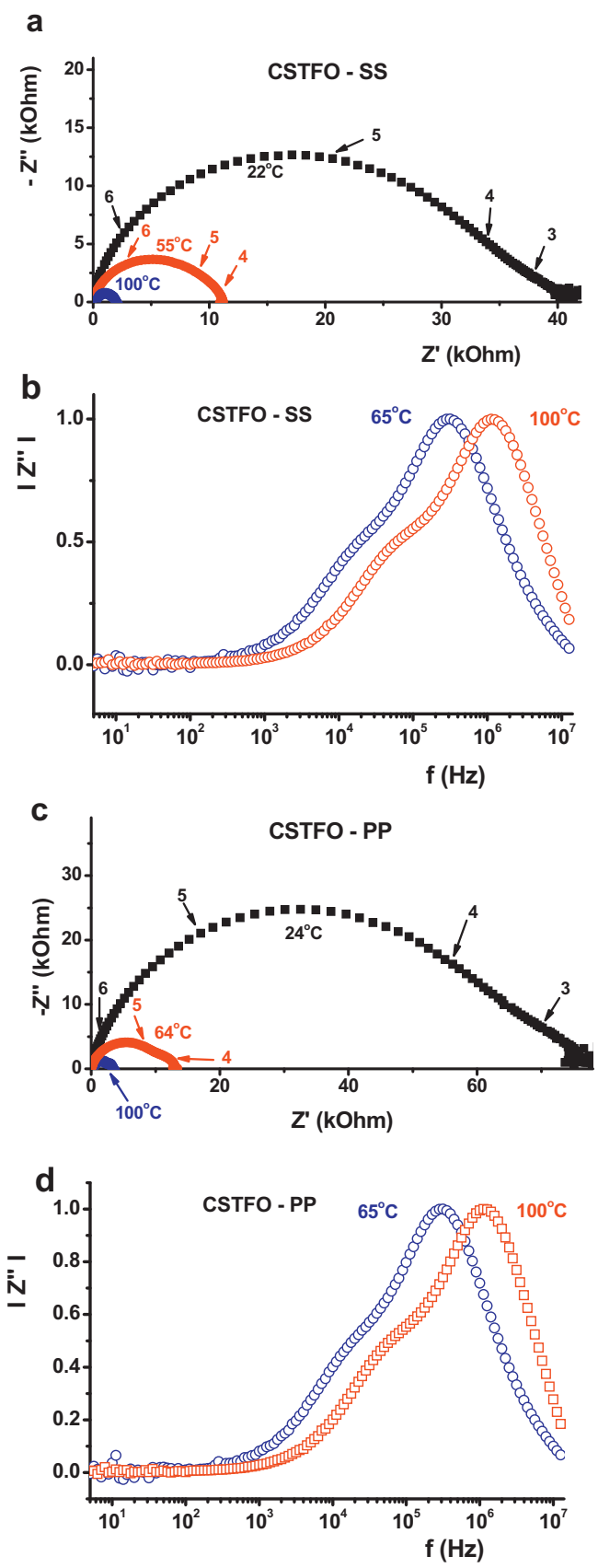

Fig. 4. (a) and (c) Impedance spectroscopy plots in the 5 Hz–13 MHz frequency range of polycrystalline $Ca_{0.5}Sr_{0.5}Ti_{0.65}Fe_{0.35}O_{3-\delta}$ (CSTFO) at several temperatures. The numbers are the logarithm of frequency. Inset: zoom of the high frequency region. (b) and (d) Bode plots at 65 and 100 °C. (a) and (b) Solid state synthesis (SS); (c) and (d) polymeric precursor (PP) technique.

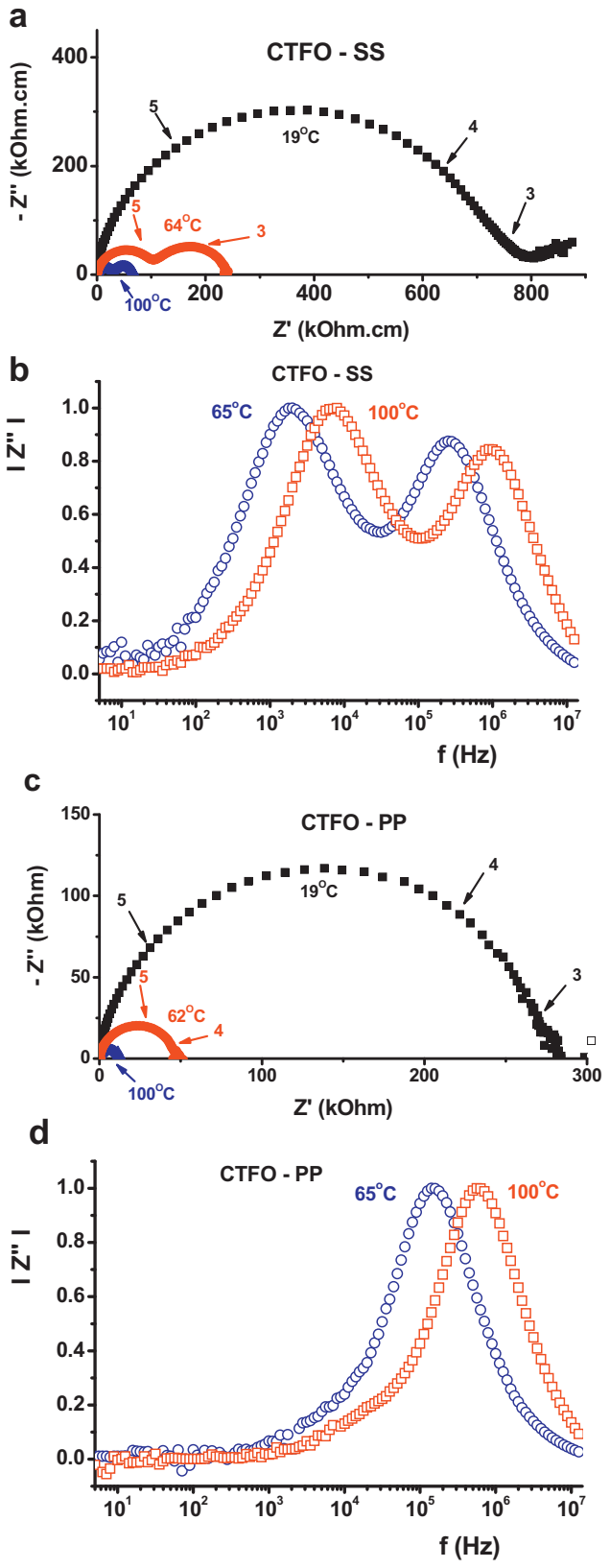

Fig. 5. (a) and (c) Impedance spectroscopy plots in the 5 Hz–13 MHz frequency range of polycrystalline $CaTi_{0.65}Fe_{0.35}O_{3-\delta}$ (CTFO) at several temperatures. The numbers are the logarithm of frequency. Inset: zoom of the high frequency region. (b) and (d) Bode plots at 65 and 100 °C. (a) and (b) solid state synthesis (SS); (c) and (d) polymeric precursor (PP) technique.

Table 1
Values of associated capacitances of grain (C_g) and grain boundary (C_{gb}) and grain boundary thickness (d_{gb}) of the sintered compounds, using powders synthesized by the polymeric precursor technique and the solid state reaction.

	C_g (10^{-11} F/cm)	C_{cg} (10^{-9} F/cm)	d_{gb} (nm)
Polymeric precursor			
$SrTi_{0.65}Fe_{0.35}O_{3-\delta}$	2.6	6.3	20
$Ca_{0.5}Sr_{0.5}Ti_{0.65}Fe_{0.35}O_{3-\delta}$	2.9	2.6	50
$CaTi_{0.65}Fe_{0.35}O_{3-\delta}$	2.6	1.3	100
Solid state reaction			
$SrTi_{0.65}Fe_{0.35}O_{3-\delta}$	1.5	1.2	220
$Ca_{0.5}Sr_{0.5}Ti_{0.65}Fe_{0.35}O_{3-\delta}$	1.7	1.7	160
$CaTi_{0.65}Fe_{0.35}O_{3-\delta}$	1.6	1.6	170

The capacitances associated to the low frequency (LF) and high frequency (HF) semicircles, evaluated using the equation $C = (RQ)^{1/\alpha}/R$ [14,15], are shown in Table 1 for the three compounds prepared with powders synthesized by the solid state synthesis and the polymeric precursor technique. Assuming 0.5 μm and 1 μm for the average grain size of the PP and SS samples, respectively, and taking into account the actual measured values of the electrode area S and the pellet thickness D of each specimen, the values of d_{gb} were evaluated according to the equation $C = C_{gb} = \varepsilon \cdot [S/d_{gb}].(d_g/D)$, with d_g and d_{gb} denoting grain size and grain boundary thickness [36,37].

The values in Table 1 are typical of specific capacitances of grains (HF) and grain boundaries (LF) capacitances [38]. Moreover, the corresponding bulk capacitances are consistent with those calculated from the bulk dielectric permittivity (approximately 300).

Fig. 6 shows, for comparison purpose, the impedance plots of the STFO, CTFO and CSTFO specimens at a chosen temperature,

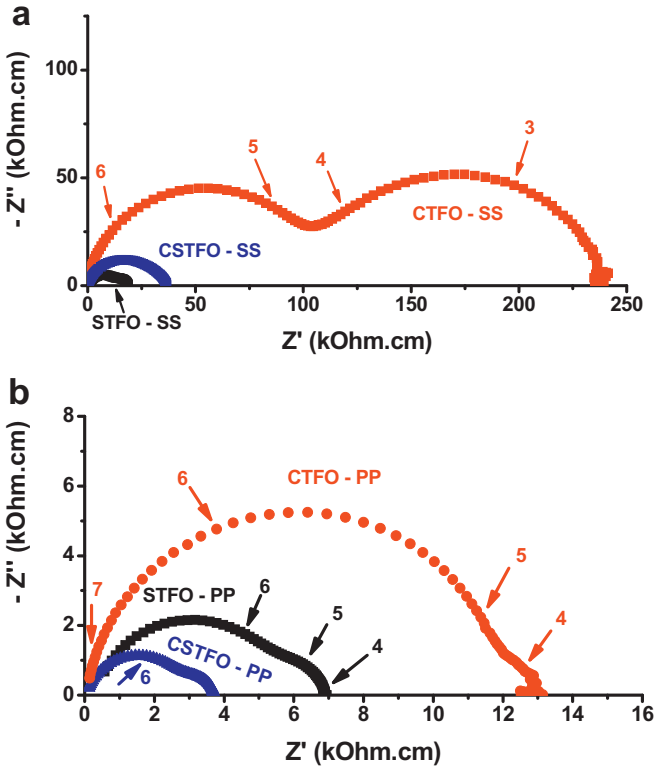

Fig. 6. Impedance spectroscopy plots in the 5 Hz–13 MHz frequency range of polycrystalline $SrTi_{0.65}Fe_{0.35}O_{3-\delta}$ (STFO), $CaTi_{0.65}Fe_{0.35}O_{3-\delta}$ (CTFO) and $Ca_{0.5}Sr_{0.5}Ti_{0.65}Fe_{0.35}O_{3-\delta}$ (CSTFO) at the same temperature, 65 °C. Inset: zoom of the high frequency region. (a) solid state synthesis (SS); (b) polymeric precursor (PP) technique.

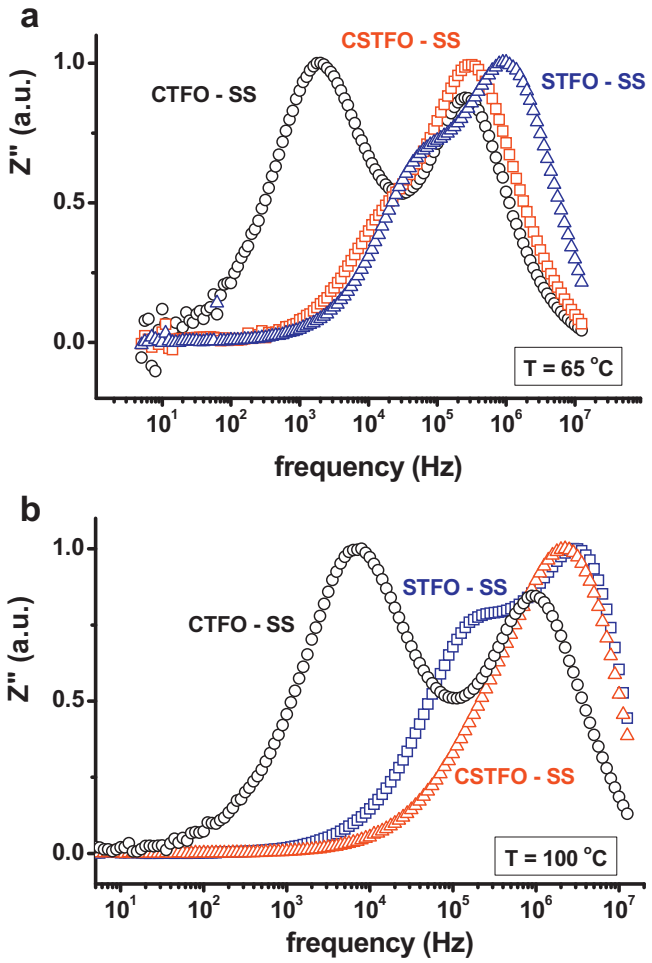

Fig. 7. Normalized Bode plots of the imaginary component of the impedance plot of $SrTi_{0.65}Fe_{0.35}O_{3-\delta}$ (STFO), $CaTi_{0.65}Fe_{0.35}O_{3-\delta}$ (CTFO) and $Ca_{0.5}Sr_{0.5}Ti_{0.65}Fe_{0.35}O_{3-\delta}$ (CSTFO) specimens, measured at 65 °C (a) and 100 °C (b). SS: solid state synthesis.

65 °C. The sequence for increasing electrical resistivity is STFO – CSTFO – CTFO for SS pellets and CSTFO – STFO – CTFO for PP pellets. The reason for the high electrical resistivity of the $CaTi_{0.65}Sr_{0.35}O_{3-\delta}$ pellets is related to the orthorhombic structure (the other two pellets are cubic), which might have a lower value of the electrical mobility due to the higher average jump distance for the oxide ion vacancy. In Fig. 7 are shown the $[|Z''| \times \log f]$ Bode plots for the STFO, CTFO and CSTFO compounds, prepared with powders obtained by solid state synthesis. Each of the Z'' data, taken at 65 °C, normalized to unity, present two maxima, corresponding to the two semicircles shown in Fig. 6. The ratios of the frequency maxima due to bulk (high frequency) and grain boundary (low frequency) relaxations are 16, 18 and 140 for STFO, CSTFO and CTFO, respectively. One may suggest that these figures are in agreement with the crystalline structures determined by X-ray diffraction, cubic perovskite for STFO and CSTFO and orthorhombic perovskite for CTFO. The average distance for the O^{2-}-vacancy hopping is smaller for the former two compounds than for the latter.

The deconvolution of the impedance plots allowed for determining the intragranular (grain) and intergranular (grain boundary) contributions to the electrical resistivity of the polycrystalline STFO, CTFO and CSTFO specimens. The Arrhenius plots are shown in Fig. 8. The activation energy is approximately 0.40 eV for the bulk and the grain boundary electrical resistivities. These values are typical of ion motion in solids and were reported for bulk conduction in Ni-doped $SrTiO_3$ (0.40 eV) [39], for

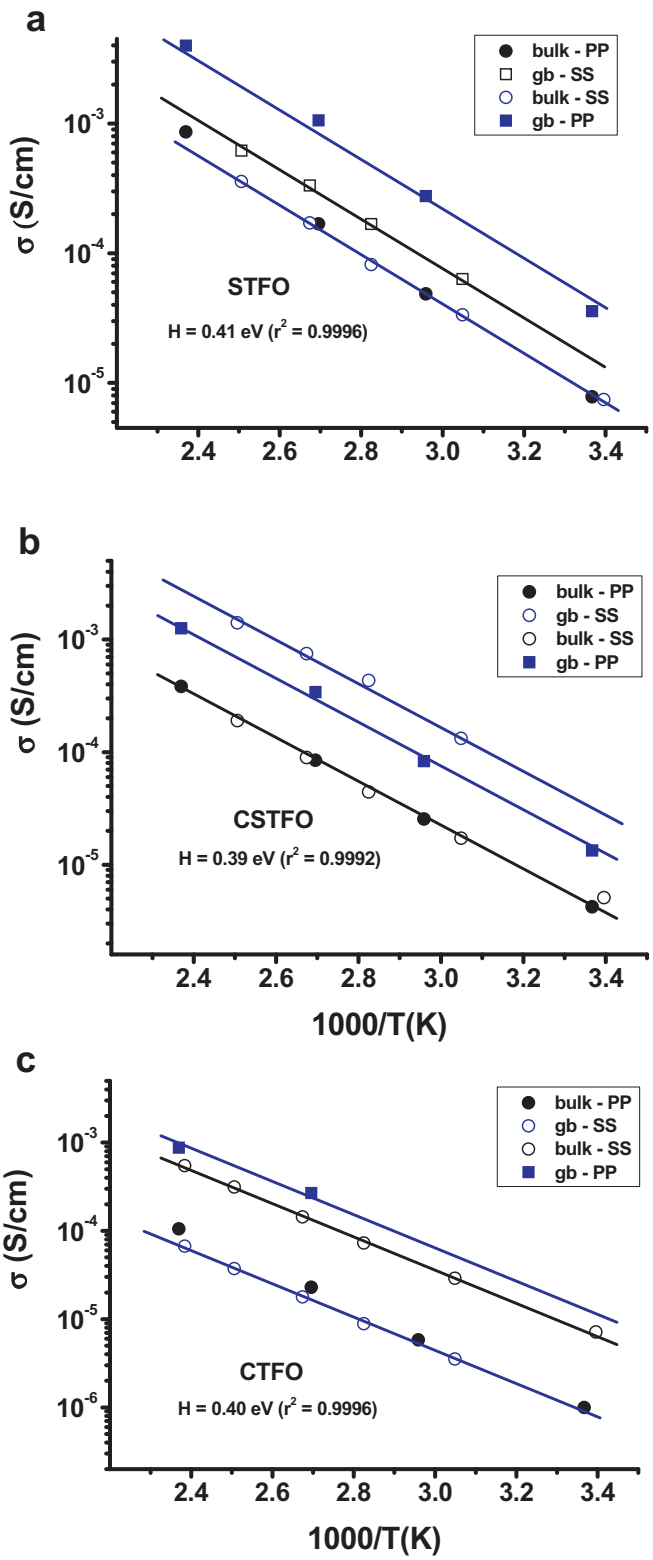

Fig. 8. Arrhenius plots of the bulk and grain boundary electrical conductivity of (a) $SrTi_{0.65}Fe_{0.35}O_{3-\delta}$ (STFO), (b) $Ca_{0.5}Sr_{0.5}Ti_{0.65}Fe_{0.35}O_{3-\delta}$ (CSTFO) and (c) $SrTi_{0.65}Fe_{0.35}O_{3-\delta}$ (STFO) compounds. SS: solid state synthesis; PP: polymeric precursor technique.

$SrTi_{0.65}Fe_{0.35}O_{3-\delta}$ thin films (0.43 ± 0.03 eV) below about 450–500 °C [40] and for $SrTi_{0.8}Fe_{0.2}O_{3-\delta}$ polycrystalline ceramics (0.39 eV) in the 100–500 °C range [41].

After the impedance spectroscopy measurements, the silver electrodes were removed from the specimens by polishing for

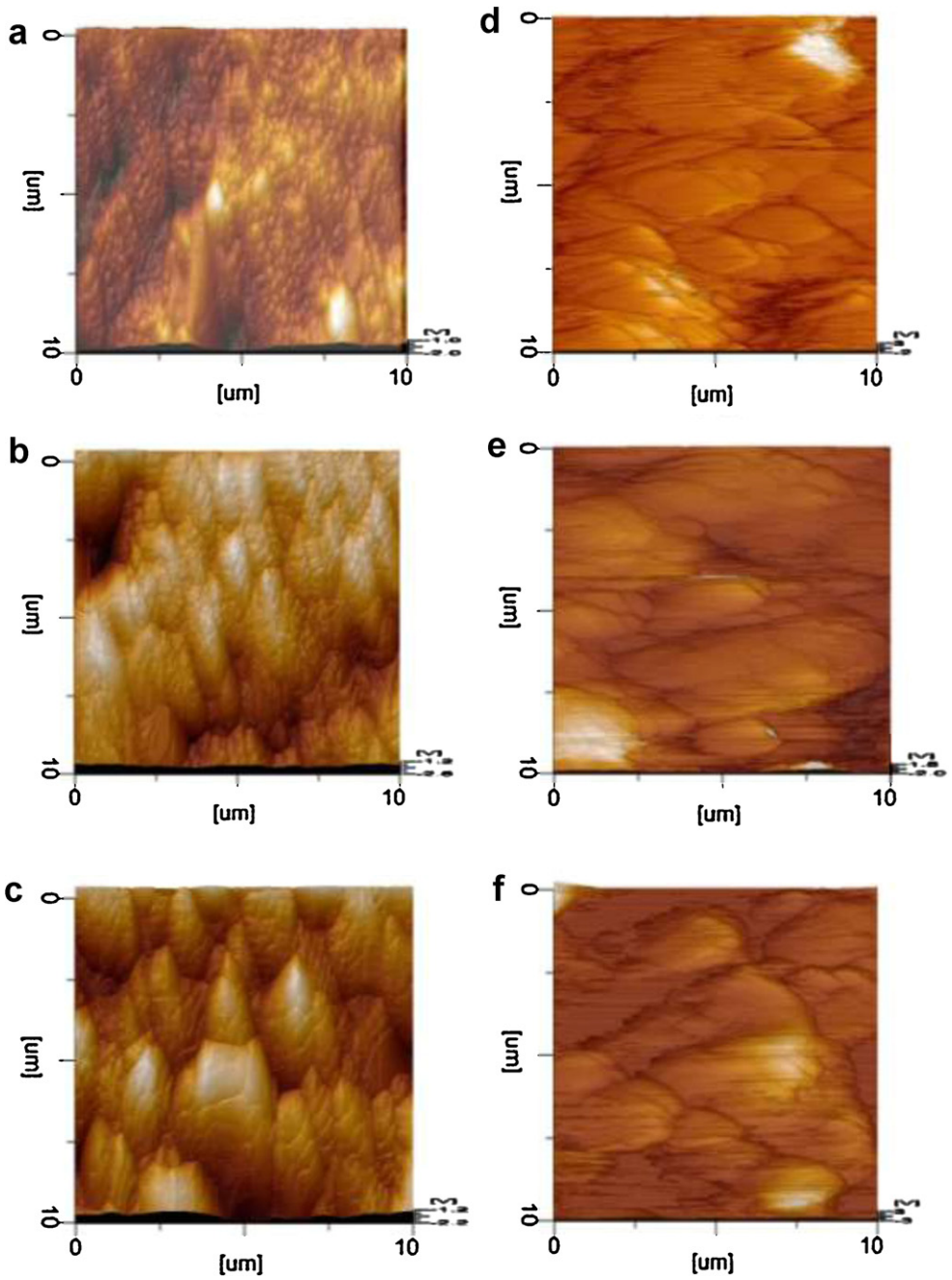

Fig. 9. Scanning probe microscopy topographic images of polished surfaces of (a) and (d) $SrTi_{0.65}Fe_{0.35}O_{3-\delta}$ (STFO), (b) and (e) $Ca_{0.5}Sr_{0.5}Ti_{0.65}Fe_{0.35}O_{3-\delta}$ (CSTFO) and (c) and (f) $Ca_{0.5}Sr_{0.5}Ti_{0.65}Fe_{0.35}O_{3-\delta}$ (CSTFO) prepared by the polymeric precursor technique (a–c) and by the solid state reaction route (d–f).

observation of the topographic images in the scanning probe microscope. Typical images are shown in Fig. 9 for the $Ca_xSr_{1-x}Ti_{0.65}Fe_{0.35}O_{3-\delta}$, $x = 0$, 0.5 and 1.0, sintered pellets prepared by the mixture of oxide and the polymeric precursor techniques. The difference the images show is striking. The specimens prepared with powders synthesized by the chemical route are highly homogeneous, dense and composed of well defined grains, such that each grain is itself composed of a large number of tightly packed sub-grains. The specimens prepared with powders synthesized by the mechanical mixing of the starting materials, on the other hand, show grains not well defined, inhomogeneous and elongated, with a large density of interfaces. These interfaces are interpreted as responsible for the blocking of charge carriers which result in the relatively large grain boundary resistivity shown in Fig. 6.

4. Conclusions

Fe substitution for Ti in $SrTiO_3$ (STFO), in $CaTiO_3$ (CTFO), and in $Ca_{0.5}Sr_{0.5}TiO_3$ (CSTFO) promotes oxide ion conduction with a similar value of intragranular (bulk) and intergranular (grain boundary) activation energy of 0.40 eV in the 300 K–500 K temperature range. Powders of these compounds, synthesized by a chemical route (polymeric precursor technique), show perovskite cubic structure for STFO, CSTFO and CTFO. Sintered pellets prepared with these powders present homogeneous grains and sub-grains, and higher electrical conductivity values. Powders prepared by the solid state synthesis, on the other hand, show the perovskite cubic structure for STFO and CSTFO, and the perovskite orthorhombic structure for CTFO. Sintered pellets prepared with these powders present non homogeneous grain size distribution

and higher electrical resistivity than the pellets prepared with powders synthesized by the polymeric precursor technique.

Acknowledgements

This work was supported by FAPESP (Grant Nos. 95/05172-4, 98/14324-0 and 05/53241-9) and CNPq.

References

[1] K. Koumoto, Y. Wang, R. Zhang, A. Kosuga, R. Funahashi, Annu. Rev. Mater. Res. 40 (2010) 363.
[2] W. Menesklou, H.J. Schreiner, K.H. Hardtl, E. Ivers-Tiffée, Sens. Actuators B 59 (1999) 184.
[3] E. Ivers-Tiffée, K.H. Hardtl, W. Menesklou, J. Riegel, Electrochim. Acta 47 (2001) 807.
[4] R. Moos, W. Menesklou, H.-J. Schreiner, K.H. Hardtl, Sens. Actuators B 67 (2000) 178.
[5] A. Rothschild, W. Menesklou, H.L. Tuller, E. Ivers-Tiffée, Chem. Mater. 18 (2006) 3651.
[6] K. Sahner, J. Straub, R. Moos, J. Electroceram. 16 (2006) 179.
[7] R. Moos, F. Rettig, A. Huerland, C. Plog, Sens. Actuators B: Chem. 93 (2003) 43.
[8] A. Rothschild, H.L. Tuller, J. Electroceram. 17 (2006) 1005.
[9] A. Rothschild, S.J. Litzelman, H.L. Tuller, W. Menesklou, T. Schneider, E. Ivers-Tiffée, Sens. Actuators B 108 (2005) 223.
[10] E. Barsoukov, J. Ross Macdonald, Impedance Spectroscopy, Theory Experiment, and Applications, 2nd ed., Wiley-Interscience, USA, 2005.
[11] J.E. Bauerle, J. Phys. Chem. Solids 30 (1969) 2657.
[12] M. Kleitz, H. Bernard, E. Fernandez, E. Schouler, in: A.H. Heuer, L.W. Hobbs (Eds.), Science and Technology of Zirconia vol. 3, The Am. Ceram. Soc. Inc., Columbus, OH, 1981, p. 310.
[13] G.J. Brug, A.L.G. Van der Eeden, M. Sluyters-Rehbach, J.H. Sluyters, J. Electroanal. Chem. 176 (1984) 275.
[14] J. Ross Macdonald, Solid State Ionics 13 (1984) 147.
[15] C.H. Hsu, F. Mansfelf, Corrosion 57 (2001) 747.
[16] S.P.S. Badwal, Solid State Ionics 76 (1995) 67.
[17] R. Waser, J. Am. Ceram. Soc. 74 (1991) 1934.
[18] R. Waser, Solid State Ionics 75 (1995) 89.
[19] S. Rodewald, J. Maier, J. Am. Ceram. Soc. 84 (3) (2001) 521.
[20] Z. Zhang, W. Sigle, R.A. de Souza, W. Kurtz, J. Maier, M. Ruhle, Acta Mater. 53 (2005) 5007.
[21] J.R. Jurado, M.T. Colomer, J.R. Frade, J. Am. Ceram. Soc. 83 (2000) 2715.
[22] J.R. Jurado, M.T. Colomer, J.R. Frade, Solid State Ionics 143 (2001) 251.
[23] D. Neagu, J.T.S. Irvine, Chem. Mater. 22 (2010) 5042.
[24] P. Blennow, K.K. Hansen, L.R. Wallenberg, M. Mogensen, Advances is Solid Oxide Fuel cells III, Ceramic Engineering and Science Proc, vol. 28, 2008, p. 203.
[25] Y. Hanajiri, H. Yokoi, T. Matsui, Y. Arita, T. Nagasaki, H. Shigematsu, J. Nucl. Mater. 247 (1997) 285.
[26] Y. Li, S. Qin, F. Seifert, J. Solid State Chem. 180 (2007) 824.
[27] A.G. Andersen, T. Hayakawa, T. Tsunoda, H. Orita, M. Shimizu, K. Takehira, Catal. Lett. 18 (1993) 37.
[28] V.M. Ferreira, F. Azough, J.L. Baptista, R. Freer, J. Mater. Res. 12 (1997) 3293.
[29] E.R. Kipkoech, F. Azough, R. Freer, C. Leach, S.P. Thompson, C.C. Tang, J. Eur. Ceram. Soc. 23 (2003) 2677.
[30] L. Zhou, P.M. Vilarinho, J.L. Baptista, J. Am. Ceram. Soc. 82 (1999) 1064.
[31] K.D. Madal, L. Behera, K. Ismail, J. Alloys Compd. 325 (2003) 309.
[32] E. Chinarro, J.R. Jurado, F.M. Figueiredo, J.R. Frade, Solid State Ionics 160 (2003) 161.
[33] R. Moos, T. Bischoff, W. Menesklou, K.H. Hardtl, J. Mater. Sci. 32 (1997) 4247.
[34] M. Kleitz, J.H. Kennedy, in: P. Vashishta, J.N. Mundy, G.K. Shenoy (Eds.), Fast Ion Transport in Solids, Elsevier/North-Holland, The Netherlands, 1979, p. 185.
[35] A.C. Larson, R.B.V. Dreele, General Structure Analysis System (GSAS), Los Alamos National Laboratory Report LAUR 86-748, 2004.
[36] J. Maier, Ber. Bunsen. Phys. Chem. 90 (1986) 26.
[37] J. Fleig, J. Maier, J. Eur. Ceram. Soc. 19 (1999) 693.
[38] J.G. Fletcher, A.R. West, J.T.S. Irvine, J. Electrochem. Soc. 142 (1995) 2650.
[39] S.-H. Yoon, C.A. Randall, K.-H. Hur, J. Appl. Phys. 107 (2010) 103721.
[40] S.J. Litzelman, A. Rothschild, H.L. Tuller, Sens. Actuators B 108 (1999) 231.
[41] S. Misra, E. Prabhu, K.I. Gnanasekar, V. Jayaraman, P. Chandramohan, M.P. Srinivasan, T. Gnanasekaran, Mater. Res. Bull. 44 (2009) 1041.